Resistive MHD Studies of High-β-Tokamak Plasmas[*]

V. E. Lynch[†]
B. A. Carreras
H. R. Hicks[†]
J. A. Holmes[†]
L. Garcia

Oak Ridge National Laboratory
Oak Ridge, Tennessee 37830

---

[*] Research sponsored by the Office of Fusion Energy, U.S. Department of Energy, under contract W-7405-eng-26 with the Union Carbide Corporation.

[†] Computer Sciences at Oak Ridge National Laboratory.

ABSTRACT

Numerical calculations have been performed to study the MHD activity in high-β tokamaks such as ISX-B. These initial value calculations built on earlier low β techniques, but the β effects create several new numerical issues. These issues are discussed and resolved. In addition to time-stepping modules, our system of computer codes includes equilibrium solvers (used to provide an initial condition) and output modules, such as a magnetic field line follower and an X-ray diagnostic code.

The transition from current driven modes at low β to predominantly pressure driven modes at high β is described. The nonlinear studies yield X-ray emissivity plots which are compared with experiment.

I. INTRODUCTION

In this paper we present theoretical models, based on the resistive MHD equations, which have been developed to study high β tokamak plasmas. A system of codes used to implement these models is also discussed along with the numerical techniques employed. The goal of this work is the study of the resistive MHD instabilities present in tokamak plasmas below the threshold of ideal instabilities. At the same time, these models have been used specifically to support and complement the experiments in the ISX-B tokamak.

The present studies at ORNL are the logical continuation of those done for low beta tokamak plasmas. This previous work included the study of internal disruptions [1], Mirnov oscillations [2], soft disruptions associated with hollow current profiles [3] and major tokamak disruptions [4]. The numerical work has always been accompanied by analytical modeling, which has uncovered some new dynamical mechanisms [5,6]. Realistic geometrical effects such as toroidicity [7] and noncircularity [8] have also been considered.

For the high β studies we have used a reduced set of resistive MHD equations [9] valid in the limit of large aspect ratio ($\varepsilon \equiv a/R_0 \ll 1$, where a and R_0 are the plasma minor and major radii respectively) and high β ($\beta \sim \varepsilon$). This system of equations with some minor variations has also been used by other groups [10,11] for similar studies. The implementatiion of these equations as an initial value problem constitutes one of the time stepping modules, RST, of the system of codes.

This system of codes consists of three types of modules (Table I): input modules, time stepping modules and output modules. The latter type includes mainly diagnostic codes. They have been used to improve the understanding of the instabilities studied. They are excellent tools for unraveling some of the characteristics of the basic dynamical mechanisms. Some output modules are used to calculate quantities, such as X-ray traces, which can be directly compared with experimental data. These diagnostic modules have been very helpful in understanding experimental data and allowing detailed comparisons between theory and experiment [12].

The equations used in the present study are discussed in Section II; and in Section III are presented the numerical methods used to advance these equations in time. A discussion of the system of codes with details on some of the diagnostic modules is given in Section IV. Finally, some results are presented in Section V.

II. EQUATIONS

Our approach to resistive MHD in moderate β tokamaks is through the use of an initial value time stepping module RST, which integrates in time a set of coupled nonlinear partial differential equations from an initial state consisting of an MHD equilibrium plus a perturbation. Theoretical studies in finite β tokamaks are generally most easily carried out in some system of flux coordinates. Since the growth of resistive instabilities frequently destroys magnetic flux surfaces, RST uses a flux coordinate system based on the MHD equilibrium. This equilibrium and the associated coordinate system are calculated using the fixed boundary code RSTEQ [13] as an input module. This code solves the axisymmetric, toroidal Grad-Shafranov equation

$$\Delta^* \Psi_{eq} \equiv R^2 \vec{\nabla}_\perp \cdot \left(\frac{1}{R^2} \vec{\nabla}_\perp \Psi_{eq}\right)$$

$$= - \frac{\beta_o}{2\epsilon^2} R^2 \frac{dp_{eq}}{d\Psi_{eq}} - \frac{1}{q^2} F_{eq} \frac{dF_{eq}}{d\Psi_{eq}} \qquad (1)$$

either in a flux conserving manner or for specified pressure and toroidal current density. All work is carried out using dimensionless equations. All lengths are normalized to a generalized plasma minor radius a, the resistivity to η_o (its value at the magnetic axis), the time to the resistive diffusion time $\tau_r = a^2\mu_o/\eta_o$ where μ_o is the vacuum magnetic permeability, the magnetic field to $B_{\zeta o}$ (the toroidal vacuum field at the plasma major radius R_o), the velocity to a/τ_r, and the pressure to p_o (its equilibrium value at the magnetic axis). In Eq. (1) the poloidal flux Ψ_{eq} is normalized to $a^2B_{\zeta o}$, β_o is the toroidal β at the magnetic axis, R is the major radius coordinate divided by R_0, the equilibrium pressure p_{eq} is a function of Ψ_{eq}, and the toroidal flux function F_{eq} is also a function of Ψ_{eq} which is normalized to $R_0 B_{\zeta 0}$.

Given dimensionless horizontal and vertical minor radii $X \equiv (R-1)/\varepsilon$ and Z, respectively, the solution of Eq. (1) can be used to define a flux coordinate system (ρ, Θ, ζ) in which ρ $(0 < \rho < 1)$ is an equilibrium flux surface variable which behaves as a generalized minor radius, Θ $(0 < \Theta < 2\pi)$ is a generalized poloidal angle variable, and ζ is the toroidal angle. The particular choice of coordinates used in RST is determined in the same way as in Ref. [14] by setting the Jacobian

$$D \equiv \frac{1}{R}\left(\frac{\partial X}{\partial \rho}\frac{1}{\rho}\frac{\partial Z}{\partial \Theta} - \frac{1}{\rho}\frac{\partial X}{\partial \Theta}\frac{\partial Z}{\partial \rho}\right)^{-1} = \frac{1}{R^{\ell}} \ , \qquad (2)$$

where the exponent ℓ determines the coordinate system. The unit of length is given by

$$a^2 = \frac{R_0^{\ell-1}}{2\pi^2} \int_V R^{-\ell}\, dV \ , \qquad (3)$$

where the integration extends over the entire plasma volume. If $\ell = 2$ is chosen in Eq. (2) then the equilibrium magnetic field lines are straight in the resulting coordinate system (Fig. 1).

In order to study resistive MHD stability and nonlinear evolution, RST employs a reduced set of 3-D resistive MHD equations derived in the limits of large aspect ratio ($\varepsilon \ll 1$) and high β ($\beta \sim \varepsilon$) [9]. In terms of the coordinate system described above, the dimensionless form of this set of equations is

$$\frac{\partial\tilde{\Psi}}{\partial t} = -\frac{1}{\rho}\frac{\partial\Phi}{\partial\theta}\frac{d\Psi_{eq}}{d\rho} - \frac{\partial\Phi}{\partial\zeta} + \frac{\partial\Phi}{\partial\rho}\frac{1}{\rho}\frac{\partial\tilde{\Phi}}{\partial\theta} - \frac{1}{\rho}\frac{\partial\Phi}{\partial\theta}\frac{\partial\tilde{\Psi}}{\partial\rho} + \eta\tilde{J}_{\zeta} \tag{4}$$

$$\begin{aligned}\frac{\partial U}{\partial t} = {} & \frac{\partial\Phi}{\partial\rho}\frac{1}{\rho}\frac{\partial U}{\partial\theta} - \frac{1}{\rho}\frac{\partial\Phi}{\partial\theta}\frac{\partial U}{\partial\rho} + S^{2}\left[\frac{\partial J_{\zeta eq}}{\partial\rho}\frac{1}{\rho}\frac{\partial\tilde{\Psi}}{\partial\theta} - \frac{1}{\rho}\frac{\partial\tilde{J}_{\zeta}}{\partial\theta}\frac{\partial\Psi_{eq}}{\partial\rho}\right.\\ & - \frac{1}{\rho}\frac{\partial J_{\zeta eq}}{\partial\theta}\frac{\partial\tilde{\Psi}}{\partial\rho} - \frac{\partial J_{\zeta}}{\partial\zeta} + \frac{\partial\tilde{J}_{\zeta}}{\partial\rho}\frac{1}{\rho}\frac{\partial\tilde{\Psi}}{\partial\theta} - \frac{1}{\rho}\frac{\partial\tilde{J}_{\zeta}}{\partial\theta}\frac{\partial\tilde{\Psi}}{\partial\rho}\\ & \left. + \frac{\beta_{0}}{\epsilon}\left(\frac{1}{R}\frac{\partial X}{\partial\rho}\frac{1}{\rho}\frac{\partial\tilde{p}}{\partial\theta} - \frac{1}{R}\frac{1}{\rho}\frac{\partial X}{\partial\theta}\frac{\partial\tilde{p}}{\partial\rho}\right)\right]\end{aligned} \tag{5}$$

$$\frac{\partial\tilde{p}}{\partial t} = -\frac{1}{\rho}\frac{\partial\Phi}{\partial\theta}\frac{\partial p_{eq}}{\partial\rho} + \frac{\partial\Phi}{\partial\rho}\frac{1}{\rho}\frac{\partial\tilde{p}}{\partial\theta} - \frac{1}{\rho}\frac{\partial\Phi}{\partial\theta}\frac{\partial\tilde{p}}{\partial\rho}\ , \tag{6}$$

where Φ is the velocity stream function, $U = \nabla_{\perp}^{2}\Phi$ is the toroidal vorticity, the resistivity $\eta(\rho)$ is taken to be constant in time, the toroidal current $J_{\zeta} = \Delta^{*}\Psi$, $\tilde{}$ denotes a perturbation quantity, and $S = \tau_{r}/\tau_{Hp}$ is the ratio of the resistive time to the poloidal Alfvén time $\tau_{Hp} = R_{0}(\mu_{0}\rho_{m})^{1/2}/B_{\zeta 0}$ where ρ_{m} is the mass density. Note that $U_{eq} = \Phi_{eq} = 0$ is assumed. The linear operator Δ^{*} in this coordinate system is

$$\begin{aligned}\Delta^{*}f \equiv {} & R^{2}D\,\frac{1}{\rho}\frac{\partial}{\partial\rho}\left[\left(g^{\rho\rho}\rho\frac{\partial f}{\partial\rho} + \rho g^{\rho\theta}\frac{1}{\rho}\frac{\partial f}{\partial\theta}\right)/R^{2}D\right]\\ & + R^{2}D\,\frac{1}{\rho}\frac{\partial}{\partial\theta}\left[\left(g^{\rho\theta}\frac{\partial f}{\partial\rho} + g^{\theta\theta}\frac{1}{\rho}\frac{\partial f}{\partial\theta}\right)/R^{2}D\right]\end{aligned} \tag{7}$$

where

$$g^{\rho\rho} = \left(\frac{1}{R\rho}\frac{\partial X}{\partial \theta}\right)^2 + \left(\frac{1}{R\rho}\frac{\partial Z}{\partial \theta}\right)^2 \tag{8}$$

$$g^{\rho\theta} = -\left(\frac{1}{R\rho}\frac{\partial X}{\partial \theta}\frac{\partial X}{R\partial \rho} + \frac{1}{R\rho}\frac{\partial Z}{\partial \theta}\frac{1}{R}\frac{\partial Z}{\partial \rho}\right) \tag{9}$$

$$g^{\theta\theta} = \left(\frac{1}{R}\frac{\partial X}{\partial \rho}\right)^2 + \left(\frac{1}{R}\frac{\partial Z}{\partial \rho}\right)^2 \; . \tag{10}$$

Equations (4)-(6) make use of the fact that Ψ_{eq} and p_{eq} are functions of ρ only. Conducting wall boundary conditions and zero pressure at the plasma edge are assumed. Although the reduced equations keep dynamical terms only to lowest order in ε, the geometric terms are kept such that the solution of the Grad-Shafranov equation (1), exact to all orders in ε, is an equilibrium for the equations (4) to (6) in the limit of zero resistivity.

The RST module advances in time equations (4) to (6) either linearly or nonlinearly as desired; it is written to solve the full nonlinear set, but linear stability calculations are also carried out by omitting the terms nonlinear in the perturbed quantities. It is also possible to switch off the pressure term in the momentum balance equation (5), while totally dropping Eq. (6). This allows the separate study of the current driven modes in a high β plasma.

III. NUMERICAL TECHNIQUES

The numerical techniques used in solving the high β equations (4), (5) and (6) are basically the same as those which were described in Ref. [15] for the cylindrical low β equations. The equations are solved using a finite difference representation in the generalized radial coordinate ρ and Fourier series expansion in the angle variable θ and ζ. In terms of this representation, quantities dependent upon the equilibrium are written

$$f_{eq}(\rho,\theta) = \sum_{m=0}^{\infty} \left[f^{c}_{eqm}(\rho) \cos m\theta + f^{s}_{eqm}(\rho) \sin m\theta \right] \tag{11}$$

while perturbation quantities are written

$$\tilde{f}(\rho,\theta,\zeta) = \sum_{n=0}^{\infty} \sum_{m=-\infty}^{\infty} \left[f^{c}_{mn}(\rho) \cos(m\theta + n\zeta) + f^{s}_{mn}(\rho) \sin(m\theta + n\zeta) \right] . \tag{12}$$

Although RST allows both sine and cosine terms, these studies have been restricted to equilibria with up-down symmetry. Then, in cases where only the cosine terms in ψ are nonzero in the initial conditions, the sine terms in ψ, and p and cosine terms in Φ remain identically zero as time evolves. In order to simplify the presentation, only this latter situation will be discussed, and the superscripts c and s will be dropped hereafter.

In practice both series (11) and (12) must be truncated at a finite number of modes. Considerable effort has been devoted to demonstrating numerical convergence [15]. Typically, 100 to 300 finite difference grid points are necessary to span the minor radius. The number of terms retained in the double sum of Eq. (12) ranges up to about 80. The most efficient selection is obtained by an ad hoc scheme [15] in which the selection of m values is dependent on n. It has been shown that, for the problems we have studied, this representation is far more efficient than a 3D finite difference grid. This gain in efficiency has been crucial in obtaining the results shown here.

Most of the numerical details can be carried over from what was discussed in Ref. [15]. However, several additional considerations necessary to RST will be discussed here. They refer mainly to the following three points: 1) the new equation (6) for the pressure which is absent at low β; 2) the problems related to matrix inversions caused by the new poloidal couplings; and 3) the choice of a coordinate system to optimize the efficiency of the calculations.

1. Numerical Treatment of the Pressure Equation

The pressure equation (6) is purely convective. It is known that centered finite difference expressions in space and time will yield two solutions, a physical one and a nonphysical one. Consider the prototype convective equation

$$\frac{\partial p}{\partial t} = v \frac{\partial}{\partial x} p \ .$$

The solution is $p(x,t) = p(x+vt, 0)$, which is a travelling wave moving in the negative x direction for $v > 0$. However, the centered finite difference form

$$\frac{p_x^{t+\Delta t} - p_x^t}{\Delta t} = v\left(\frac{p_{x+\Delta x/2}^{t+\Delta t/2} - p_{x-\Delta x/2}^{t+\Delta t/2}}{\Delta x}\right)$$

has two independent solutions [16]. This arises because there are two uncoupled grids, one at $n\Delta t$, $m\Delta x$, and one at $(n + 1/2)\Delta t$, $(m + 1/2)\Delta x$. This gives rise not only to the physical solution, but also to a spurious backward moving one. Taking a one-sided space difference

$$p_{x+\Delta x} - p_x \text{ or } p_x - p_{x-\Delta x}$$

solves this problem, but the choice of form is dictated by the local sign of v. This procedure is called up-wind differencing and is due to R. Lelevier [17]. An equivalent representation [18] is obtained by a centered discretization of

$$\frac{\partial p}{\partial t} = v \frac{\partial}{\partial x} p + |v| \frac{\Delta x}{2} \frac{\partial^2 p}{\partial x^2} \; ,$$

where a diffusion term has been added.

When Eqs. (4)-(6) are solved using centered finite differences in Eq. (6), pressure profiles such as those in Fig. 2a can result. The non-physical solution can lead to a shock front as can be seen in the figure (near r = 0.58). The second term in (6) does couple the grids, but there is no guarantee that it is large enough. Up-wind differencing of the last term in (6) is impractical since it is obtained by convoluting the two factors. Instead, a diffusive term

$$\chi\Delta^* p$$

is added. Three forms for γ have been used,

$$\gamma = \gamma_0 \tag{13}$$

$$\gamma = \gamma_0 \, \eta_\perp(\rho) \tag{14}$$

$$\gamma = \gamma_0 \frac{\Delta\rho}{2} \, |v_\rho(\rho,t)| \tag{15}$$

where γ_0 is a specified constant. We have taken $\eta_\perp(\rho)$ proportional to the parallel resistivity. Form (14) (Fig. 2b) is suggested by the close connection between the pressure and the toroidal magnetic field, which has $\eta_\perp$ as its coefficient of diffusion. With proper choice of γ_0, this is sufficient to remove the shock front from the solution. Form (15) is suggested by the above argument concerning equating a diffusion term with an up-wind differencing scheme. This gives a diffusion coefficient which is not only dependent on minor radius, but also is a strong function of time, since generally, the velocity is growing. This technique has a similar effect (Fig. 2c), with the advantage that the diffusive term is of small magnitude until it is needed.

C. Matrix Inversions

Another important difference between the high β and low β numerical schemes is in the form of the matrices required to calculate the inversion of $U = \Delta_\perp^2 \Phi$ and the implicit diffusion terms $\eta\Delta^* \psi$ in Eq. [illegible] and $\gamma\Delta^* p$, which is added into Eq. [illegible] as described above. Because the high β toroidal equilibria lack poloidal symmetry, Fourier components having a given toroidal mode number n, but different poloidal mode numbers m are linearly coupled through equilibrium quantities. Using a three point second order radial difference scheme, a block tridiagonal matrix having MJ × MJ blocks (MJ being the number of radial grid points) with each block of size M(n) × M(n) (where M(n) is the number of poloidal components of toroidal mode number n in the calculation) must be inverted for each toroidal mode number n in each of the three operations alluded to above. In addition to adding complexity to the matrix structure for the Δ^* and related operators, these geometric couplings necessitate the inclusion of a greater number of Fourier components in order to represent the modes. This has the effect of shortening the time step size used by RST as can be seen from the formula

$$\Delta t < \frac{2}{S \, \mathrm{Max} \left| n - \frac{m}{q(\rho)} \right|} \qquad (6)$$

which results from a simplified von Neumann stability analysis of Eqs. (4) and (5).

In RST the block tridiagonal matrix solutions require more computer time than any other part of the code. Because of the large number of Fourier components, the shortness of the time step, and the dominance of the matrix equations in computer time, it is essential to use efficient software for their solution. RST solves the matrix equations using the block tridiagonal matrix package BT RTMC [[illegible]]. In order to increase the speed of the code we have tested an approximation technique in which each block in the block tridiagonal matrix is replaced by its diagonal. For each toroidal mode number n this reduces the block tridiagonal matrix to M(n) simple tridiagonal matrices of length MJ. These matrices no longer explicitly couple different components of toroidal mode number n, though such couplings remain in other terms in the equations. The effect of the couplings in the approximate matrix terms can be introduced into this scheme by iterating the approximate matrix with the full inverse operator of the block tridiagonal matrix in an appropriate fashion. In cases for which the approximate matrix scheme converges, the answers agree well with those obtained using the full block tridiagonal scheme, even without iteration.

3. Choice of Coordinate System

Variation of the coordinate system was attempted to obtain a more compact representation, in terms of Fourier components, of the modes in the high β regime. Such an approach, using $\ell=1$ rather than $\ell=2$, which is the natural choice for tearing mode studies, has been suggested in Ref. [14]. The effect is to shift the poloidal coordinate grid more toward the outside (in major radius) of the plasma, and hence to "put more coordinates" in the region of steep pressure gradients where balooning modes should occur. For the resistive balooning modes studied with RST, the change from $\ell=2$ to $\ell=1$ was found to have no effect in improving the poloidal representation of the modes. This is shown in Fig. 3, where we plot magnetic and pressure energy norms, by

$$E_{\psi mn} = \frac{1}{2}\int_0^1 \rho d\rho \left[\left(\frac{\partial\psi_{mn}}{\partial\rho}\right)^2 + \left(\frac{m\psi_{mn}}{\rho}\right)^2\right] \qquad (17)$$

and

$$(E_p)_{mn} = \int_0^1 \rho d\rho \; P_{mn} \quad . \tag{18}$$

for an n=1 eigenmode as functions of the poloidal mode number n. Although this case is for a high β equilibrium ($\varepsilon\beta_p$ = 1.1), the ℓ=2 straight field line coordinate system is seen to provide at least as economical a representation of the poloidal structure of the mode as does ℓ=1. Because of these tests, we generally use ℓ=2 in our calculations.

IV. SYSTEM OF CODES

The system of resistive MHD codes (Table I) is constructed to efficiently use the results of the major modules. The present major nonlinear time-stepping modules include RSF [15] (low β cylindrical geometry) and RST with toroidal geometry. The latter can run both low β and high β, circular and noncircular cases. To begin a sequence of runs with RST for noncircular or high β cases, an appropriate equilibrium must first be generated with RSTEQ [13]. At specified times, both modules dump save files and also standard diagnostic print and plot files. These save files can be used not only to initialize the major modules for continuation runs, but also as input to any of the modules in the diagnostic system. Since these files are permanently stored and the modules maintain the capability to read previous save files, the diagnostic system is capable of analyzing any previous run.

The diagnostic system consists of a magnetic field line module, a stability package of Δ' solvers, a statistical package called DINOS which calculates correlation functions and other statistical information and a package that computes experimental information such as X-ray signals and $\tilde{B}_\theta/B_\theta$. Here we will describe the experimental package and the field line module which are the most relevant for the high β calculations.

The experimental package simulates X-ray detector signals in ISX-B using save files from the major modules. The line integral of the X-ray emissivity is modeled as the line integral of the pressure squared and either toroidal or poloidal rotation of the mode structure at constant frequency is assumed (Fig. 4). Realistic geometry for the three X-ray arrays in ISX-B (Fig. 5) is used to simulate experimental results. The intersection of each chord in the arrays with the edge of the plasma must first be found for the limits of integration. These limits are found by searching over equal steps in θ around the plasma edge and using interpolation between steps. The trapezoidal rule is used to integrate the X-ray emissivity, I, where

$$I(\rho\Theta,t) = g\left[\sum_{m,n} F_{mn}(\rho t)\cos(m(\omega_p t + \Theta) + n(\zeta + \omega_T t))\right]^2$$

g = normalization constant

ω_T = frequency of toroidal rotation

ω_p = frequency of poloidal rotation

$f_{mn}(\rho,t)$ = interpolation in ρ and t of $p_{mn}(\rho_i,t_i)$.

Since I is a function of ρ and Θ and we take equal steps along the chords in X and Z coordinates, we must invert:

$$X = \sum_m x_m(\rho) \cos m\Theta$$

$$Z = \sum_m z(\rho) \sin m\Theta .$$

HYBRD1 [20], a zero-finder for systems of nonlinear equations, is used for this inversion. We use linear interpolation in ρ and SPLINF and SEVAL [21] to spline fit in t to find $f_{mn}(\rho,t)$. The integral of I and the maximum of I are then computed at given times and plotted for each chord (Fig. 6). The code also plots the X-ray emissivity in three dimensions (Fig. 4).

The experimental package also computes the poloidal magnetic field fluctuations at the plasma boundary, $\tilde{B}_\theta/B_\theta$. Due to the complex geometry of the Mirnov coils in ISX-B, we do not use realistic geometry in these calculations. Instead we use detectors that are equally spaced poloidally. Using ZEROIN [21], a combination of the bisection and secant methods, we find the corresponding 0 at the edge of the plasma. Then we use divided differences to compute

$$\frac{\tilde{B}_\theta}{B_\theta} = \frac{\sum\limits_{mn} \left.\frac{\partial \psi_{mn}}{\partial \rho}\right|_{\rho=1} \cos(m(\omega_p t + 0) + n(\zeta + \omega_T t))}{\left.\frac{\partial \psi_{00}}{\partial \rho}\right|_{\rho=1}}$$

If $\psi_{mn}(\rho,t)$ is known for multiple times we spline fit in t. The phase of these fluctuations is found by searching for the first peak in the fluctuation for each detector and plotting the poloidal angles of the detectors vs $\omega\Delta t$ of the first peak.

The experimental package runs in approximately five minutes on the Cray-1. The X-ray emissivity is integrated at 200 times for each X-ray detector chord for 32 side chords and two arrays of 24 top chords. The number of steps across each chord is a function of the chord length with a maximum of one hundred steps. Three dimensional plots of the X-ray emissivity are drawn at four different times on a 39 by 39 grid. Poloidal magnetic field fluctuations are calculated for 64 detectors.

The field line module integrates the magnetic field line equations using ψ from the save files of the major codes. DE [22], a software integration package is used to integrate the equations:

$$\frac{d\rho}{d\zeta} = \frac{1}{\rho F} \sum_{mn} m\psi_{mn}(\rho) \sin(m\Theta + \zeta)$$

$$\frac{d\Theta}{d\zeta} = \frac{1}{\rho F} \sum_{mn} \frac{d\psi_{mn}(\rho)}{d\rho} \cos(m\Theta + n\zeta) \ .$$

For given $\rho(\zeta_0)$ and $\Theta(\zeta_0)$. DE uses a modified divided difference form of the Adams Pece formulas and local extrapolation. It adjusts the order and stepsize automatically. Note that in the field line equations, since a Fourier series expansion is used for the angle varibles Θ and ζ, only one dimensional interpolation is required. Puncture plots at different toroidal angles are produced (Fig. 7) showing the magnetic field line structure at a given time.

V. RESULTS

A large number of calculations have been done to assess the dependence of the high β resistive instabilities on different equilibrium parameters. The mode of operation has been to generate, for a fixed q-profile parameterized as

$$q(\rho) = q_0[1 + (\rho/\rho_0)^{2\lambda}]^{1/\lambda} \tag{19}$$

and pressure profile $p(\psi) = (\psi(\rho)/\psi(0))^2$, a flux conserving sequence of equilibria by increasing β_0. Many such sequence have been studied. They have been selected by changing either q_0 or $q(\rho=1)$ for a given plasma cross section shape. In this way we can separate the pressure effects from shear effects. Sequences with different plasma shape have also been studied in circular, elliptical, D and square cross sections. Detailed analysis of these effects on the (m=1; n=1) mode will appear elsewhere [23]. Sequences of equilibria which closely resemble some of ISX-B discharge parameters have also been studied. This has allowed detailed comparisons with the measured MHD activity in ISX-B [12].

From the point of view of linear stability properties, we shall describe here the results for a particular flux conserving equilibrium sequence. These results are typical of such sequences. The equilibria are characterized by a q-profile with $q(0) = 1.34$, $\lambda = 2$ and $\rho_0 = 0.60$. The calculations were performed for a tokamak with aspect ratio 10. At low β and in the cylindrical limit the (m=3; n=2) tearing mode is the only *n=2 linearly unstable mode. Using the linear equations, the n=2* linear growth rate is calculated for several equilibria with increasing β_0. The results are shown in Fig. 8 (continucus line). In the same figure is plotted the growth rate for the n=2 mode when the pressure term is removed from Eq. (5) (broken line). For the latter calculation, β affects the instability only through the equilibrium. This result shows that the current driven component of the instability is strongly stabilized when β increases in a flux conserving manner. It is important to underline the last condition. When a flux conserving sequence of equilibria is generated, the equilibria are deformed in such a way that the toroidal peak in the current shifts further to the outside than does the magnetic axis. The separation between the current peak and the magnetic axis increases with β. In this way, the q=1.5 singular surface moves toward smaller current gradient as β increases. This, of course, stabilizes the current driven part of the mode. However, when pressure effects are added to the momentum balance equation, the overall effect is an increase of the growth rate (Fig. 8, continuous line). Therefore the pressure effects are destabilizing and the mode is mostly driven by pressure. The n=2 mode changes from a pure tearing mode at low β to a pressure driven mode at high β. The structure of the eigenfunction (Fig. 9) shows the increasing ballooning character of this mode.

Higher n modes, for instance the n=5 mode, are stable in the low β cylindrical limit. They are destabilized by finite β effects and their linear growth rate increases with β. They show features typical of ballooning modes, but current driving effects are still important for such modes as the n=5. This can be seen in Fig. 10, where the different Fourier components of the n=5 pressure eigenfunction are plotted. The higher m components show the typical high n ballooning structure. However, the low m components have a more complicated structure due to the current driving terms.

The change in the character and structure of the linear eigenfunctions has an important bearing on the nonlinear behaviour of the instabilities. Furthermore, the increased number of couplings among the Fourier components increases the complexity of the nonlinear evolution and structure of these modes. To gain a clear understanding, it is therefore helpful to consider a simple situation, such as an equilibrium sequence which, in the low β cylindrical limit, is unstable to a single tearing mode. We can look at the effects of β, toroidicity and noncircularity as a modification of this basic mode. This picture makes sense if these effects are small. If they are large the whole mode structure changes, as discussed above. Because of the abundance of m=1 MHD activity in high β experiments [12], it is interesting to focus attention on the (m=1; n=1) mode. The change in the nonlinear behaviour of this mode with increasing β has been summarized in Fig. 11. This figure shows the m=1/n=1 magnetic island width evolution versus time (top) and the evolution of the (m=2; n=1) component of the poloidal magnetic field at $\rho=1$ (bottom) for several equilibria belonging to the same flux conserving sequence. The growth of the m=1/n=1 island slows down with increasing β, going from exponential to linear growth in time, before reconnection takes place. For the equilibrium with the highest β value shown in Fig. 11, the m=1/n=1 island saturates without full magnetic field line reconnection. This change of the nonlinear behaviour happens when the n=1 mode is mainly driven by pressure. For this particular equilibrium sequence, the largest driven mode is the (m=2; n=1) mode. This component produces a large poloidal field fluctuation at $\rho=1$ (Fig. 11, bottom). This can be seen as a measure of the coupling due to β effects and used to correlate with experiment. Many other components are also driven by the ($m=1$; $n=1$) mode through equilibrium and nonlinear couplings. Of this broad spectrum of modes, some generate magnetic islands which, in many cases, overlap and break magnetic surfaces. This is illustrated in Fig. 7, which shows a snapshot of the magnetic field line configuration before reconnection takes place. Four poloidal planes are shown for the same instant of time. The case shown in Fig. 7 corresponds to an ISX-B-like equilibrium, and includes noncircular, toroidal and finite β effects. Figure 4 shows the X-ray emissivity for the same case at the same time. These results have been successfully used to reproduce the ISX-B MHD activity for some discharges [12].

The nonlinear evolution of the resistive instabilities at high β is sensitive to the value of S. Moreover, the resulting solution can be qualitatively different at low S ($S < 10^4$) from that at high S($S > 10^5$). There are two particular instances for which this is abundantly clear. The nonlinear evolution of the ($m=1$; $n=1$) mode can change from saturation to reconnection when S increases. This effect is illustrated in Fig. 12 which shows the evolution of the $m=1/n=1$ island width for $S=10^4$ and $S=10^5$ for a particular equilibrium. Therefore, for comparison with experiment, it is important to be sure that the value of S used in the calculations is sufficiently high, in order to be in the right regime.

It is also very important to use an adequate value of S in studying the nonlinear behaviour of the high n pressure driven modes. For low values of S these modes do not saturate and they cause a strong singularity in the pressure. At higher values of S ($S \simeq 10^6$) they tend to saturate at a low level.

ACKNOWLEDGMENT

We thank R. A. Dory for presenting these [illegible]s at the Wildhaus Conference. We also thank Julian Dunlap and his collaborators for their assistance.

It is a pleasure to thank Janice Hughes for the accurate and rapid typing of this manuscript.

One of us (L.G.) appreciates the financial support of the U.S. - Spanish Joint Committee for Scientific and Technical Cooperation.

REFERENCES

[1] Jahns, G. L., Soler, M., Waddell, B. V., Callen, J. D., Hicks, H. R., Nucl. Fusion 18 (1978) 609.

[2] Carreras, B. A., Waddell, B. V., Hicks, H. R., Nucl. Fusion 19, (1979) 1423.

[3] Carreras, B. A., Hicks, H. R., Waddell, B. V., Nucl. Fusion 19, (1979) 583.

[4] Waddell, B. V., Carreras, B. A., Hicks, H. R., Holmes, J. A., Phys. Fluids 22 (1979) 896; Carreras, B. A., Hicks, H. R., Holmes, J. A., Waddell, B. V., Phys. Fluids, 23 (1980) 1811.

[5] Carreras, B. A., Rosenbluth, M. N., Hicks, H. R., Phys. Rev. Letters 46 (1981) 1131.

[6] Hazeltine, R. D., Diamond, P. H., Carreras, B. A., Hicks, H. R., "Renormalized Tearing Mode Turbulence and Major Disruption," Annual Controlled Fusion Theory Conference, Austin, Texas, 1981, paper 3A2.

[7] Carreras, B. A., Hicks, H. R., Lee, D. K., Phys. Fluids 24 (1981) 66.

[8] Carreras, B. A., Holmes, J. A., Hicks, H. R., Lynch, V. E., Nucl. Fusion 21 (1981) 511.

[9] Strauss, H. R., Phys. Fluids 20 (1977) 1354.

[10] Monticello, D. A., Park, W., Jardin, S. C., Chance, M. S., Dewar, R. L., White, R. B., Grimm, R. C., Manickam, J., Strauss, H. R., Johnson, J. L., Greene, J. M., Glasser, A. H., Kaw, P. K., Rutherford, P. H., Valeo, E. J., in Plasma Physics and Controlled Nuclear Fusion Research edited by I.A.E.A., Vienna 1981 Vol. I, p. 359.

[11] Edery, D., Pellat, R., Soule, J. L., "Equations for the Nonlinear Evolution of Resistive Tearing Modes in Toroidal Plasmas," Report EUR-CEA-FC-[illegible] (1979).

[12] Dunlap, J. L., Carreras, B. A., Paré, V. K., Holmes, J. A., Bates, S. C., Bell, J. D., Hicks, H. R., Lynch, V. E., Navarro, A. P. (to be published).

[13] Holmes, J. A., Peng, Y-K. M., Lynch, S. J., J. Comput. Phys. 36 (1980) 35.

[14] Dewar, R. L., Manickam, J., Grimm, R. C., Chance, M. S., Princeton Plasma Physics Laboratory Report PPPL-1663.

[15] Hicks, H. R., Carreras, B. A., Holmes, J. A., Lee, D. K.,

Waddell, B. V., Oak Ridge National Laboratory Report ORNL/TM-[illegible]32 (1979) (to be published in J. Comput. Phys.).

[16] Potter, David, "Computational Physics", edited by John Wiley and Sons, New York (1973).

[17] Richtmyer, Robert D., Morton, K. W., "Difference Methods for Initial-value Problems," Interscience Publishers, New York, 1967, p. 292.

[18] Roberts, K. V., Potter, D. E., "Magnetohydrodynamic Calculations," in *Methods in Computational Physics*, [illegible], *Plasma Physics*, edited by Alder, B., Fernbach, S. and Rotenberg, M., New York/London: Academic Press, p. [illegible].

[19] Hindmarsh, A. C., "Solution of Block-Tridiagonal Systems of Linear Algebraic Equations," Lawrence Livermore Laboratory Report UCID-30150 (1977).

[20] Garbow, B. S., Hillstrom, K. E., Moré, J. J., Minpack Project, Argonne National Laboratory (1980).

[21] Forsythe, G. E., Malcolm, M. A., Moler, C. B., "Computer Methods for Mathematical Computations," Prentice Hall, New Jersey (1977).

[22] Shampine, L. F., Gordon, M. K., "Computer Solution of Ordinary Differential Equations: The Initial Value Problem," W. H. Freeman and Co., San Francisco (1975).

[23] Holmes, J. A., Carreras, B. A., Hicks, H. R., Lynch, V. E., Rothe, K. E., "Finite β Effects on the Nonlinear Evolution of the (m=1; n=1) Mode in Tokamaks," ORNL/TM-[illegible] (to be published).

FIGURE CAPTIONS

Fig. 1. Coordinate system. Lines of constant ρ and θ are shown for the case $\ell=2$.

Fig. 2. Pressure profile across a horizontal minor diameter of the plasma showing the effect of various pressure equation diffusion terms.
Top: no diffusion ($\kappa_0 = 0$); Middle: resistivity-dependent diffusion, Eq. (14) with $\gamma_0 = 0.3$; Bottom: velocity-dependent diffusion, Eq. (15) with $\kappa_0 = 10.0$.

Fig. 3. Falloff of the magnetic energy and pressure terms with poloidal mode number for an $n=2$ linear eigenmode calculated using coordinate systems having $\ell=1$ and $\ell=2$.

Fig. 4. X-ray emissivity at four times in a single poloidal plane with a toroidal rotation imposed.

Fig. 5. Geometry of the three arrays of X-ray detectors on ISX-B. They are in a single poloidal plane.

Fig. 6. X-ray signals produced by the initial value calculation.

Fig. 7. Field line plot on four poloidal planes.

Fig. 8. Linear growth rate of the $n=2$ eigenfunction. The dashed line shows the effect of the current driving terms alone, the pressure terms having been removed.

Fig. 9. Poloidal view of the $n=2$ linear eigenfunction, showing the change in character as β/ϵ is increased.

Fig. 10. Radial distribution of the components of the $n=5$ pressure eigenfunction for $\beta/\epsilon = 0.38$.

Fig. 11. Transition from reconnection (at low β_p) to saturation (at higher β_p) is shown by the evolution of the $m=1/n=1$ island width and the ($m=2$; $n=1$) poloidal magnetic field fluctuation at the plasma boundary.

Fig. 12. In differentiating reconnection cases from saturation cases, low values of S do not necessarly give the same result as high values of S.

TABLE I

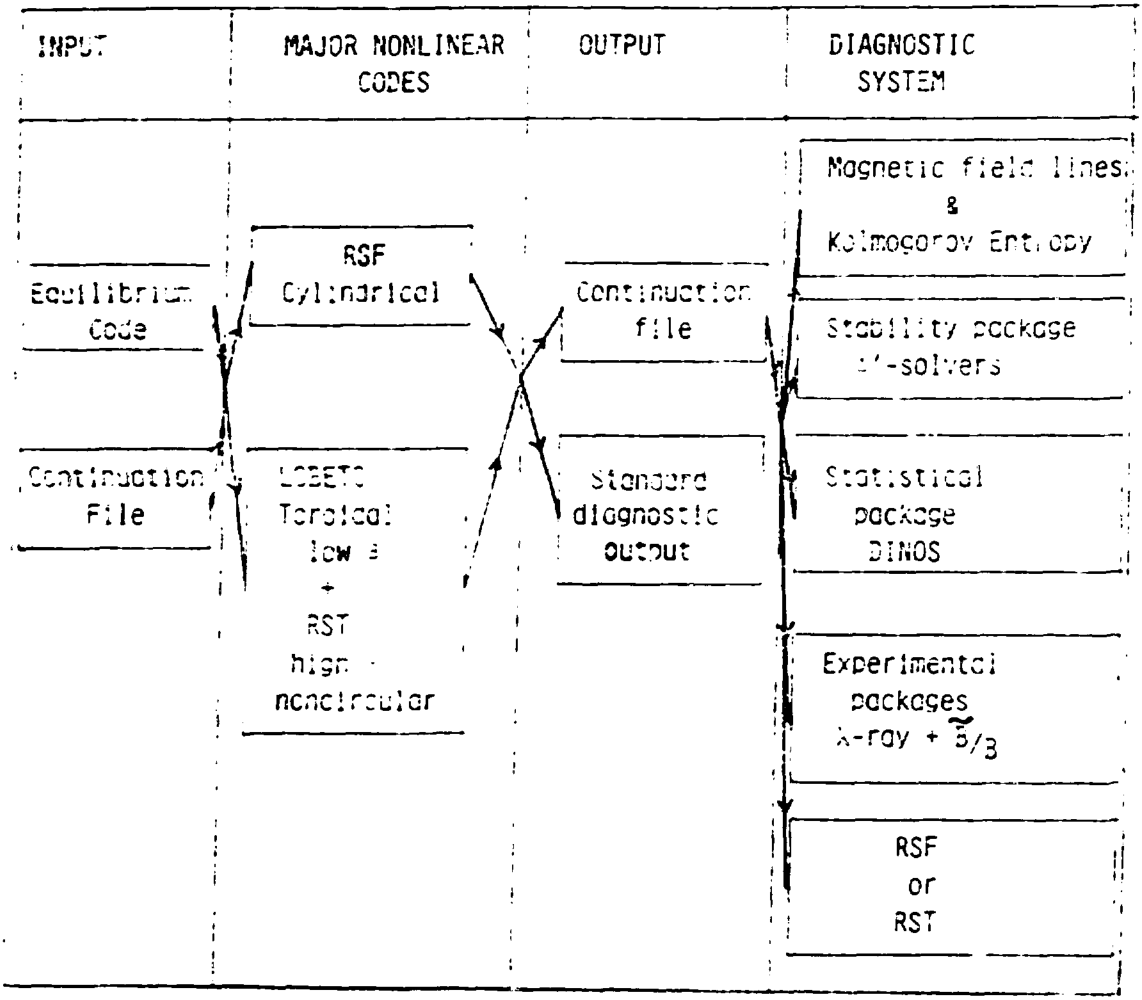

INPUT	MAJOR NONLINEAR CODES	OUTPUT	DIAGNOSTIC SYSTEM
			Magnetic field lines & Kolmogorov Entropy
Equilibrium Code	RSF Cylindrical	Continuation file	Stability package Δ'-solvers
Continuation File	LOBETO Toroidal low β + RST high β noncircular	Standard diagnostic output	Statistical package DINOS
			Experimental packages X-ray + $\tilde{B}/B$
			RSF or RST

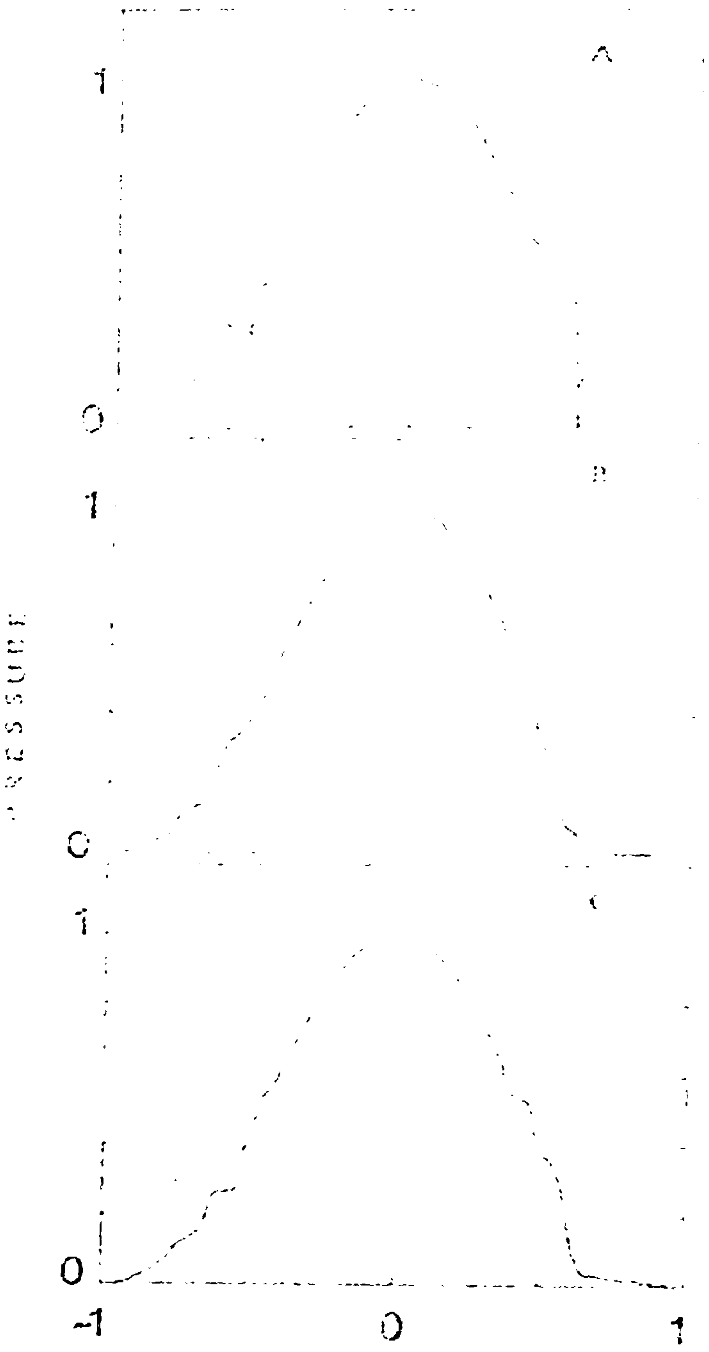
A
B
C
PRESSURE
1
0
1
0
1
0
-1
0
1

32 DETECTORS


24
28
32
36